International Journal of Applied Earth Observation and Geoinformation 149 (2026) 105289

Contents lists available at ScienceDirect

International Journal of Applied Earth Observation and Geoinformation

journal homepage: www.elsevier.com/locate/jag

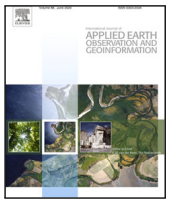

Hyperspectral assessment of wheat lodging: From field to EnMAP satellite observations

Mehmet Furkan Celik [a,*], Padmageetha Nagarajan [b], Andrew Nelson [a], Zaib Unnisa [c], Booker Ogutu [c], Jadunandan Dash [c], Mirco Boschetti [d], Ewelina Dobrowolska [e], Espen Volden [f], Roshanak Darvishzadeh [a]

[a] Faculty of Geo-Information Science and Earth Observation (ITC), University of Twente, Enschede, 7522 NH, The Netherlands
[b] Department of Geographical Sciences, University of Maryland, College Park, MD 20742, United States
[c] School of Geography and Environmental Science, University of Southampton, Southampton, SO17 1BJ, United Kingdom
[d] Institute for Electromagnetic Sensing of the Environment (IREA), National Research Council of Italy (CNR), Milano, 20133, Italy
[e] European Space Agency (ESA/ESRIN), Frascati, 00044, Italy
[f] Serco c/o ESA-ESRIN, Directorate of Earth Observation Programmes, Frascati, 00044, Italy

ARTICLE INFO

Keywords:
Crop lodging
Wheat
Remote sensing
Hyperspectral
EnMAP
Machine learning
Spectral feature importance

ABSTRACT

Crop lodging, the permanent displacement of crop stems from their vertical position, causes substantial yield and quality losses in wheat production. Early and accurate detection of lodging and its severity is therefore essential for improving harvest management and reducing economic risk. This study, for the first time, examines hyperspectral data from the Environmental Mapping and Analysis Program (EnMAP) satellite in conjunction with field hyperspectral measurements and machine learning algorithms to detect wheat lodging and its severity and to identify spectral regions important for lodging detection. The study was conducted at Bonifiche Ferraresi Farm in Italy, where wheat biophysical measurements were collected alongside spectral measurements acquired using an Analytical Spectral Device (ASD) spectroradiometer, concurrent with EnMAP data acquisition. Wheat spectral reflectance derived from both field and EnMAP data was analyzed to determine how lodging alters wheat spectral characteristics and to identify sensitive wavelengths. Following spectral preprocessing, lodging severity was quantified using a lodging score and modeled with Principal Component Analysis (PCA) based Gaussian Process Regression (GPR), Partial Least Squares Regression (PLSR), Multilayer Perceptron (MLP), and Explainable Boosting Machine (EBM). Model performances and spectral relevance were evaluated through PCA loadings, Variable Importance in Projection (VIP), SHapley Additive exPlanations (SHAP) values, and EBM feature contributions. The results indicate that EBM achieved the highest predictive performance (R^2 = 0.66 and ϵ_{rmse} = 0.15 for ASD and R^2 = 0.60 and ϵ_{rmse} = 0.18 for EnMAP), while interpretability analyses consistently highlighted six key spectral regions (550, 670, 720–740, 865, 1650, and 2130–2190 nm) as being sensitive to lodging-caused structural changes in wheat canopies. These findings demonstrate the potential of hyperspectral modeling for satellite-based lodging assessment under cloud-free acquisition conditions, while highlighting current constraints on operational deployment related to revisit frequency, atmospheric effects, and transferability beyond the study site and growth stage.

1. Introduction

High demand in agriculture often leads to the overuse of fertilizers and water resources in an effort to boost crop yields. Cereal crops are fundamental components of human nutrition, serving as a significant food source. In 2023, maize, wheat and rice alone accounted for 91% of total global cereal production (FAO, 2024). As such, their vulnerability to environmental pressure is especially concerning. Heavy rains, intense winds, and the simultaneous inefficient use of fertilizers and irrigation may pose additional risks to the stability of cereals resulting in reductions in crop productivity and quality. Lodging, which is the permanent displacement of a crop's stem from its vertical position (Pinthus, 1974), is a major cause of losses in cereal production. Lodging can occur anywhere between the stem elongation to ripening growth stage, with crops becoming more susceptible at later growth stages (Rajkumara, 2008). Lodging in cereal crops, particularly wheat, can result in substantial yield losses at the field level, up to 75% (Berry and Spink,

* Corresponding author.
E-mail address: m.f.celik@utwente.nl (M.F. Celik).

https://doi.org/10.1016/j.jag.2026.105289
Received 3 February 2026; Received in revised form 22 March 2026; Accepted 7 April 2026
Available online 11 April 2026

2012). Early detection of lodging and its severity is critical, as lodging may significantly decrease crop quality and yield. Real-time or near-real-time availability of such information is crucial for enhancing estimates of crop yield losses, informing insurance loss adjusters, and guiding management decisions throughout the season or for subsequent seasons.

Conventional techniques for detecting and assessing crop lodging primarily rely on field observations and physical models developed in the field or laboratories. Physical models were initially developed to simulate the lodging of crops caused by wind (Baker, 1995) and later expanded to quantitatively model the risk of lodging for wheat (Baker et al., 1998, 2014). However, these models can only be deployed in a limited and sparsely distributed manner, even with optimization, due to their high data requirements, complexity, point-based nature, and high computational costs. The most popular strategies for detecting and evaluating lodging severity are field-based methods based on visual examination (Chauhan et al., 2019). However, these techniques are expensive and impractical for regions greater than a few hundred hectares and depend on the observer's expertise, experience, and reliability.

Remote sensing plays an important role in assessing and monitoring crop and soil parameters. The spectral and backscatter behaviors of plant canopies are altered by changes in their biochemical and biophysical properties, canopy architecture and soil background (Darvishzadeh et al., 2008; Darvishzadeh, 2025). Hence, remote sensing-based estimation of these parameters enables the detection of lodging and its severity during critical growth stages. For instance, time-series analysis of remote sensing data has been successfully applied to detect lodging in wheat using a lodging score index that integrates crop angle of inclination and lodged area (Chauhan et al., 2020c).

Advances in remote sensing, including optical and radar systems, now enable periodic and timely information on crop conditions across large and remote areas. Despite major progress in satellite-based crop monitoring, studies specifically addressing crop lodging detection and severity assessment remain limited. Consequently, developing robust methods for lodging detection and severity assessment remains an important research need. Several types of remote sensing imagery have been used to detect and characterize lodging. Synthetic Aperture Radar (SAR) has been used to monitor the extent and severity of lodging in crops like maize, wheat, and rice by leveraging its sensitivity to changes in crop structure (Yang et al., 2015; Han et al., 2017; Chauhan et al., 2021; Dai et al., 2022; Qu et al., 2023). However, SAR-based lodging detection can be confounded by crop properties such as biomass, making it difficult to isolate lodging effects from other factors without careful modeling or time-series analysis. Furthermore, heterogeneous lodging patterns and the limited ability of some SAR metrics to capture subtle orientation changes reduce the reliability of lodging severity estimation at field scale (Chauhan et al., 2020a,b).

Multispectral data complement SAR by capturing visible and near-infrared reflectance, enabling the development of spectral indices that help distinguish lodged from healthy crops. Several studies have used multispectral data from airborne systems, UAVs and satellite systems to detect lodging. Balloon and low-altitude platforms have been used to derive canopy-height and thermal/NIR cues for lodging assessment, although height can be biased near harvest (Murakami et al., 2012; Chapman et al., 2014). UAV studies combining visible–NIR bands with textural features can achieve high classification accuracies, though confusion with bare soil is an issue when textures are similar (Liu et al., 2014; Yang et al., 2017). At the satellite scale, relatively few studies have used multispectral satellite imagery (e.g., Sentinel-2, Gaofen-1, and Gaofen-2) to assess lodging in wheat and maize (Chauhan et al., 2020c; Guan et al., 2022; Chen et al., 2022; Tang et al., 2022; Zhang et al., 2026). The combination of multispectral data and SAR has proven to be particularly effective in crop lodging detection, as it merges the structural insights provided by SAR with the spectral richness of multispectral data. This fusion of data sources has led to more accurate and reliable lodging detection and mitigated the effects of crop lodging on yield (Wang et al., 2020; Guo et al., 2023)

Compared to multispectral sensors, hyperspectral sensors measure reflectance in many narrow, closely spaced wavelengths rather than a handful of broad bands. This richer spectral detail can capture more subtle crop responses and help to investigate lodging-related signals across the full spectral range (400–2500 nm). Further utilizing hyperspectral data allows overcoming the spectral saturation problem and the limited sensitivity of multispectral data to subtle canopy structural or biochemical changes (Mutanga and Skidmore, 2004). To date, hyperspectral research on lodging has been concentrated at the field and UAV scales, where high spectral resolution can be paired with detailed ground observations. For example, field hyperspectral measurements have been used to distinguish lodged from non-lodged rice, with lodging primarily affecting the magnitude of the reflectance response across the measured spectrum (Liu et al., 2011). UAV-based hyperspectral studies have extended this work to maize, however, these analyses were restricted to the visible-near infrared domain (400–900 nm), where high-resolution spectra from this domain were used to characterize lodging stress and to evaluate post-lodging recovery patterns (Sun et al., 2022, 2024). Longer-term in situ hyperspectral datasets have also been used to evaluate spectral indices for rice lodging detection (Sarker et al., 2026). However, despite these advances, spaceborne hyperspectral applications remain comparatively limited, and to the best of our knowledge, no studies have yet used hyperspectral satellite data to explicitly assess lodging severity. Furthermore, it is still uncertain which spectral features best support lodging detection and severity assessment from hyperspectral satellite data, and how these features compare with those derived from field-based hyperspectral measurements.

Although lodging has traditionally been inferred from optical reflectance and SAR backscatter, often using derived metrics such as vegetation indices and texture measures (where available) (Yang et al., 2015; Han et al., 2017; Chauhan et al., 2020a), recent studies increasingly rely on machine learning and deep learning for improved lodging assessment. Most approaches operationalize "severity" in two main ways: (i) segmenting lodged areas (used as a proxy for severity) using encoder–decoder and transformer-style segmentation models (Zhang et al., 2020; Zhao et al., 2020; Jiang et al., 2022; Yu et al., 2023; Zhao et al., 2023; Zhang et al., 2023) and (ii) classifying lodging into severity grades, which is addressed in a small number of studies using dedicated severity-focused frameworks (Ali et al., 2023; Azizi et al., 2024; Zang et al., 2024). These recent studies, which primarily rely on UAV multispectral (and RGB) imagery and SAR data, highlight a gap that hyperspectral, particularly spaceborne hyperspectral, approaches remain underused for deriving quantitative, biophysically meaningful lodging severity estimates that are robust across individual settings.

In this context, different machine learning strategies offer complementary advantages for hyperspectral lodging assessment. Linear latent-variable methods such as PLSR remain useful for handling collinear spectral predictors and for deriving wavelength importance measures, whereas nonlinear models such as GPR and MLP can better capture complex reflectance–lodging relationships. Interpretable methods such as EBM are particularly relevant where predictive performance must be complemented by transparent attribution of informative spectral regions. These considerations motivated the combination of linear, nonlinear, and interpretable machine learning models evaluated in this study (Rosipal and Krämer, 2005; Williams and Rasmussen, 1995; Murtagh, 1991; Nori et al., 2019; Celik et al., 2023).

Therefore, this study investigates hyperspectral remote sensing at both satellite and field scales to detect wheat lodging and quantify its severity, and identifies the spectral bands most informative for lodging detection using hyperspectral satellite (EnMAP) and field (ASD spectrometer) data. To this end, we employ machine-learning modeling, two-band vegetation indices (TBVI), and continuum-removed spectra to characterize lodging-sensitive spectral behavior and to assess the degree of overlap in informative wavelength regions across sensors.

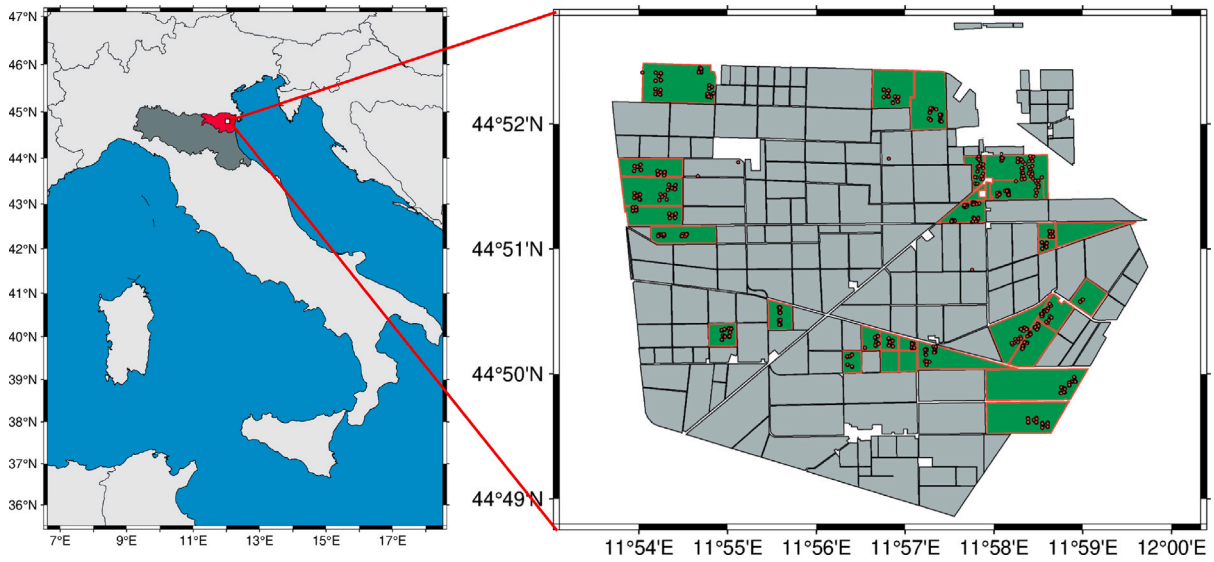

Fig. 1. Location of the study site, Bonifiche Ferraresi Farm in Italy. Left: Location of the study region (red area) in northern Italy. Right: Detailed map of the study area (44°49′–44°52′ *N*, 11°54′–12°00′ *E*), showing cadastral parcels of wheat fields (green fields outlined in red), and individual sampling points (red dots).

2. Materials

2.1. Study area

The farm owned by Bonifiche Ferraresi, an agri-food company with one of the largest agricultural holdings in Italy, was selected as the research site to monitor and detect wheat lodging. Located in the province of Ferrara, within the Emilia-Romagna region, the study area is situated in the municipality of Jolanda di Savoia and comprises approximately 3850 ha of arable land (Fig. 1). The area is characterized by a warm temperate climate suitable for a wide range of crops. Bonifiche Ferraresi cultivates wheat, barley, corn, rice, soybeans, and other horticultural and forage crops, which are typically managed under multi-year crop rotation systems. Winter wheat is generally sown between late October and early November and harvested by the end of June; from May onward, particularly during the grain-filling phase following flowering, the crop is highly susceptible to lodging. During the 2022–2023 growing season, three wheat types were cultivated over a total area of 664.24 ha: emmer wheat (Triticum dicoccum), durum wheat (Triticum durum), and soft wheat (Triticum aestivum).

A field campaign was conducted from April 30 to May 18, 2023, during the flowering period, to collect field biophysical parameters and hyperspectral measurements for lodging score estimation in the wheat fields. During this period, wheat was in the flowering stage, which falls within the broader growth interval during which lodging susceptibility increases (Rajkumara, 2008). The sampling sites were selected using a stratified random sampling design to capture the observed range of lodging severity across the study area while reducing bias toward particular parcels or easily accessible locations. This approach was intended to ensure representation of healthy, moderately lodged, and severely lodged conditions across the sampled wheat fields. The sampling was carried out on two spatial scales corresponding to field and satellite remote sensing data. Given EnMAP's 30 m spatial resolution, a 90 m × 90 m plot was defined to enable extraction of the hyperspectral remote sensing signal using a 3 × 3 pixel window. Within each 90 m × 90 m plot, fifteen 1 m × 1 m microplots were sampled, clustered around the plot's corners and center, to capture within-plot variability of biophysical and spectral parameters on a fine spatial scale (Fig. 2(a)). This configuration was intended to provide discrete within-plot observations rather than continuous spatial coverage of the full 90 m × 90 m area. The final number of microplots reported in Table 1 reflects the subset of valid measurements retained after quality control and plot-level aggregation.

These microplots provided insights into lodging biophysical characteristics (slant height and crop inclination angle), and variability at the smallest spatial scale. Each parameter was evaluated at the microplot level. Subsequently, the measurements were averaged at plot levels to generate parameters across the two spatial scales.

2.2. Field data collection

The crop angle of inclination (CAI), the angle between the stem and ground in relation to the vertical, provides a quantitative measure of lodging (Chauhan et al., 2020a). To calculate the CAI within the microplot, crop vertical height (h_{vl}), distance from the canopy head to the soil surface and the slant height (h_{sl}), distance from the canopy head to the point where lodging begins (see Fig. 2(b)) were measured using tape measure readings taken within each microplot. These values were then used to calculate the CAI according to Eq. (1):

$$\mathrm{CAI}(\theta) = 90^\circ - \arcsin\left(\frac{h_{vl}}{h_{sl}}\right) \tag{1}$$

The lodging score (LS) classifies the severity of lodging in a given area. The LS calculation incorporated both CAI and visual assessments of the lodged area (LA), providing a normalized score for comparative analysis (Chauhan et al., 2020b) (Eq. (2)). Here, LA represents the visually estimated lodged area percentage within each 1 m × 1 m microplot, expressed on a 0%–100% scale. It was assessed in the field as the proportion of the microplot area covered by plants that were permanently displaced from the vertical position.

$$\mathrm{LS} = \left(\frac{\mathrm{LA}}{100}\right)\left(\frac{\mathrm{CAI}(\theta)}{90^\circ}\right) \tag{2}$$

Here, CAI(θ) denotes the crop angle of inclination (in degrees), h_{vl} is the vertical height from the canopy head to the soil surface, and h_{sl} is the slant height from the canopy head to the point where lodging begins. LA denotes the visually estimated lodged area within each microplot, expressed as a percentage on a 0–100 scale. LS is the resulting lodging score.

The LS range is used to categorize plots into;

- Healthy: $0 \leq \mathrm{LS} \leq 0.05$
- Moderately lodged: $0.05 < \mathrm{LS} \leq 0.35$
- Severely lodged: $0.35 < \mathrm{LS} \leq 0.90$

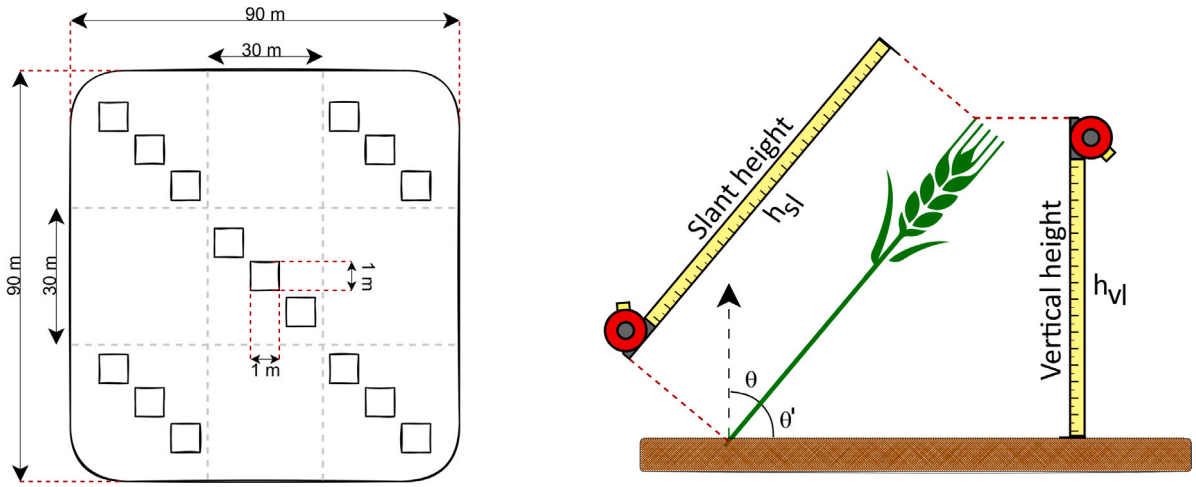

(a) Sampling strategy for field sample collection.

(b) Illustration of the variation in crop height and crop inclination angle with lodging.

Fig. 2. Overview of field sampling and crop lodging characteristics. Panel (a) is a conceptual schematic of the sampling design (not drawn to area scale). Within each 90 m × 90 m plot used for 3 × 3 EnMAP extraction, fifteen discrete 1 m × 1 m microplots were sampled to characterize within plot variability in lodging and spectral response.

This classification system provided a basis for evaluating spectral reflectance and other remote sensing parameters concerning crop health and lodging. To derive plot-level measurements, values from the microplots were averaged.

2.3. Remote sensing data

2.3.1. Enmap hyperspectral image

The EnMAP hyperspectral satellite mission, managed by the German Aerospace Center (DLR), is designed to monitor and analyze Earth's environment on a global scale. EnMAP operates in a sun-synchronous orbit, providing high-resolution hyperspectral data that captures detailed information across a wide range of wavelengths. The satellite is equipped with a hyperspectral imager that consists of 224 spectral bands, covering the visible and near-infrared (VNIR) range from 420 to 1000 nm and the shortwave infrared (SWIR) range from 900 to 2450 nm. This spectral coverage allows for precise analysis of environmental parameters. The EnMAP satellite has a ground swath width of 30 kilometres, revisiting the same location every 27 days at the equator, with more frequent coverage at higher latitudes. EnMAP data products are available at different processing levels 1B, 1C, and 2 A, each with different processing procedures. This study used a level 2 A product (radiometric, geometric, and atmospheric errors corrected). A cloud-free EnMAP hyperspectral image acquired on 21 May 2023 and obtained from DLR (German Aerospace Center) was selected for this study, as it represented the closest cloud-free satellite observation to the field campaign period. EnMAP reflectance represents an area integrated satellite signal and is influenced by solar illumination and sensor viewing geometry in addition to atmospheric correction uncertainties. In contrast, the ASD measurements were acquired under near-nadir field geometry and a much smaller instantaneous field of view. Therefore, cross-sensor differences may partly reflect BRDF-related effects and scale mismatch, not only differences in spectral sampling.

For the 21 May 2023 acquisition, the EnMAP metadata reported a solar zenith angle of 25°, solar azimuth angle of 170°, viewing zenith angle of 11°, and viewing azimuth angle of 14°.

2.3.2. Field hyperspectral measurements

An Analytical Spectral Device spectrometer was used to measure the spectral reflectance of the canopy for both healthy and lodged wheat at the microplot level. The spectroradiometer operates within a wavelength range of 350 nm to 2500 nm, with a spectral sampling interval of 1 nm. The instrument comprises three sensors: VNIR (350 nm to 1000 nm), SWIR 1 (1000 nm to 1800 nm), and SWIR 2 (1800 nm to 2500 nm). The spectroradiometer was calibrated in each microplot using a reference white panel before data collection. An optical fiber probe with a 25° field of view was positioned vertically downward at a height of 1 m above the wheat canopy. Ten consecutive measurements were recorded at each microplot to minimize noise and reduce randomness. Measurements were conducted exclusively on sunny days under clear-sky conditions. A total of 189 microplot-level spectral reflectance measurements were acquired using the specified protocol (Table 1.)

Table 1
Number of microplots and plots by Wheat Status.

Wheat status	Nr. of microplots	Nr. of plots
Healthy	74	23
Lodged	115	41

2.4. Data preprocessing

The data preprocessing workflow (Fig. 3), details the steps undertaken for both data sources, the implementation of multiple analytical methods, and the presentation of the obtained results. For field spectral measurements and EnMAP hyperspectral data, several steps were taken to enhance data quality. Noisy bands (350–400 nm and 2350–2500 nm) were removed due to the high levels of instrument-related noise and water vapor absorption regions (1340–1420 nm and 1800–1960 nm) were excluded to reduce atmospheric interference. Outliers were identified using the Interquartile Range (IQR) criterion by removing those falling outside the 25%–75% range to ensure consistency. Following outlier removal, the mean spectral reflectance was calculated within each microplot and plot to provide a reliable representation of average spectral behavior. A Savitzky-Golay filter, with a 2-degree polynomial applied across a 9-wavelength window, was used to smooth the spectral data, effectively reducing noise while preserving critical spectral features (see Fig. 4). These preprocessing steps ensure that each data source contributes reliably to the overall analysis, enhancing the accuracy of remote sensing-based applications in environmental studies.

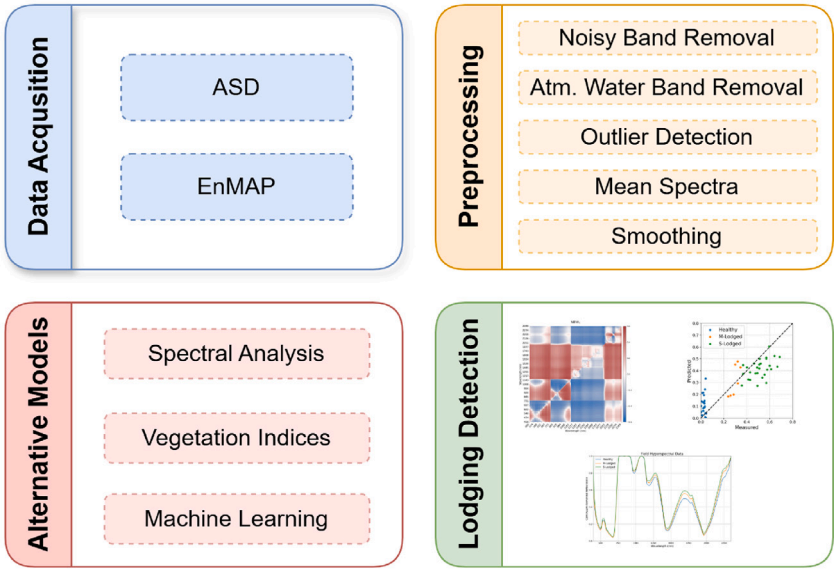

Fig. 3. Workflow: data acquisition → preprocessing → modeling → evaluation of lodging detection.

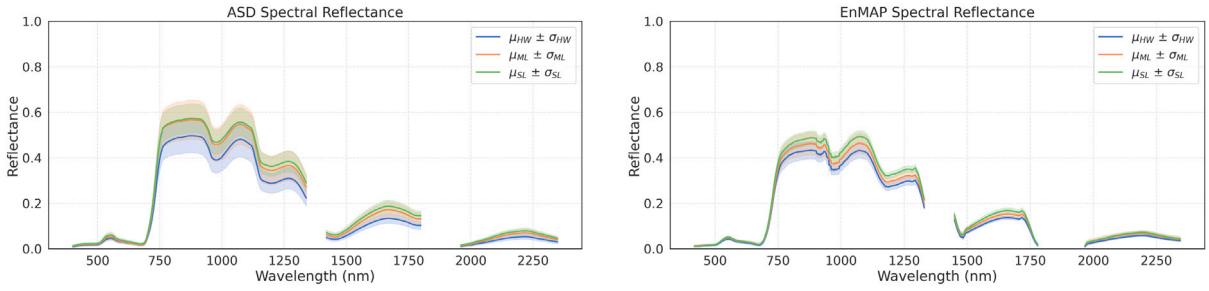

Fig. 4. Analysis-ready spectral reflectance data obtained after preprocessing, (a) ASD field measurement, (b) EnMAP data, showing the reflectance values prepared for further analysis and modeling. Each color corresponds to the lodging occurrence level.

3. Methods

We detected and identified wheat lodging from hyperspectral reflectance using three complementary analysis levels with increasing modeling complexity. First, continuum removal was applied as a physically motivated preprocessing step to normalize reflectance and emphasize diagnostic absorption features for direct spectral interpretation. Second, two-band vegetation indices (TBVI) were used as a simple and widely adopted approach to screen wavelength-pair interactions and to identify sensitive spectral regions across the full wavelength domain. Third, supervised machine learning pipelines were employed to quantify lodging severity from high-dimensional spectra and to capture potentially nonlinear relationships that are not well represented by individual absorption features or index-based measures. Methods were compared using three accuracy metrics, and we analyzed which absorption features and wavelength regions most strongly relate to lodging.

3.1. Continuum removal

We applied continuum removal (Kokaly and Clark, 1999) to normalize reflectance and emphasize discrete absorption features associated with canopy structural changes due to lodging. Let $R(\lambda)$ be the reflectance at wavelength λ and $H(\lambda)$ the convex-hull continuum. The continuum-removed reflectance is

$$R_c(\lambda) = \frac{R(\lambda)}{H(\lambda)}. \tag{3}$$

We define absorption depth and area as

$$D(\lambda) = 1 - R_c(\lambda), \qquad A_B = \int_B \big(1 - R_c(\lambda)\big)\, \mathrm{d}\lambda, \tag{4}$$

for band interval B.

3.2. Two-band vegetation indices (TBVI)

We computed ratio-based TBVI across the VIS–NIR–SWIR spectrum (Mutanga and Skidmore, 2004) and screened wavelength pairs for lodging sensitivity while mitigating soil/background effects. For wavelengths λ_1, λ_2 with reflectances $R(\lambda_1), R(\lambda_2)$, we used the normalized difference form

$$\mathrm{TBVI}(\lambda_1, \lambda_2) = \frac{R(\lambda_1) - R(\lambda_2)}{R(\lambda_1) + R(\lambda_2)}. \tag{5}$$

We generated λ–λ performance maps by fitting each TBVI to lodging labels and plotting the resulting Pearson correlation $r(\lambda_1, \lambda_2)$ over the wavelength grid.

3.3. Principal component analysis (PCA) based Gaussian process regression (GPR)

To address high dimensionality in hyperspectral data, we first applied PCA for unsupervised compression and then modeled the resulting principal-component (PC) scores with GPR (Jolliffe and Cadima, 2016;

Table 2
Hyperparameter optimization for each ML algorithm using predefined search space and selected values.

Method	Hyper-parameter	Search space	Selected
GPR	C	0.1–2.0	1.54
	Length	0.1–2.0	0.66
	Noise	0.01–0.5	0.10
EBM	Learning rate	0.0001–0.1	0.01
	Estimators	3–200	120
	Max depth	5–90	10
	Min sample split	2–30	4
	Min samples leaf	1–10	5
MLP	Hidden layers	1–3	2
	Neuron size	16–128	32, 16
	Activation fn.	ReLU/Tanh/Logistic	ReLU
	Optimizer	Adam/SGD	Adam
	Learning rate	0.0001–0.1	0.003
	α	0.0001–0.01	0.0007

Williams and Rasmussen, 1995). Given mean-centered spectra $X \in \mathbb{R}^{n\times p}$,

$$X \approx ZP^{\top}, \qquad Z = XP_k, \tag{6}$$

where $P_k \in \mathbb{R}^{p\times k}$ contains the top-k loading vectors and $Z \in \mathbb{R}^{n\times k}$ are the corresponding PC scores. In addition to reducing dimensionality for efficient GPR training, PCA supports wavelength-level interpretation through the PC loadings, which indicate the relative contribution of each wavelength to the dominant modes of spectral variability.

We modeled the target y using a zero-mean Gaussian process,

$$f(\cdot) \sim \mathcal{GP}\big(0,\, k(\cdot,\cdot)\big), \qquad y = f(Z) + \varepsilon,\ \ \varepsilon \sim \mathcal{N}(0, \sigma^2 I), \tag{7}$$

with a radial basis function kernel $k(z_i, z_j) = \alpha^2 \exp\big(-\frac{1}{2}\|z_i - z_j\|^2/\ell^2\big)$, where α^2 is the signal variance, ℓ the characteristic length scale, and σ^2 the noise variance.

3.4. Partial least squares regression (PLSR)

We employed PLSR for supervised dimension reduction and regression, well-suited to collinear hyperspectral predictors (Rosipal and Krämer, 2005). Let predictors $X \in \mathbb{R}^{n\times p}$ and response $y \in \mathbb{R}^n$. PLSR decomposes

$$X = TP^{\top} + E, \qquad y = Tq + f, \tag{8}$$

where $T \in \mathbb{R}^{n\times a}$ are scores, $P \in \mathbb{R}^{p\times a}$ loadings, and $q \in \mathbb{R}^a$ the y-loadings for a components. With weight matrix $W \in \mathbb{R}^{p\times a}$, the regression vector and predictions are

$$\hat{\beta} = W\,(P^{\top}W)^{-1}q, \qquad \hat{y} = X\hat{\beta}. \tag{9}$$

To assess predictor relevance with respect to the response variable, we employed the Variable Importance in Projection (VIP) metric derived from PLSR. VIP summarizes each predictor's overall contribution across the retained latent components, weighting components by the amount of response variance they explain. For a PLSR model with p predictors and A components, the VIP score for predictor j is given by

$$\mathrm{VIP}_j = \sqrt{p\,\frac{\sum_{a=1}^{A} \mathrm{SSY}_a \dfrac{w_{ja}^2}{\sum_{k=1}^{p} w_{ka}^2}}{\sum_{a=1}^{A} \mathrm{SSY}_a}},$$

where w_{ja} is the X-weight of predictor j on component a, and SSY_a is the variance in Y accounted for by component a (summed over responses for multivariate Y). Larger VIP scores indicate greater overall importance.

3.5. Multilayer perceptron (MLP)

We trained an MLP directly on high-dimensional spectra to capture nonlinear and nonadditive relationships (Murtagh, 1991). For input $x \in \mathbb{R}^p$, the network computes

$$h^{(1)} = \phi\big(W^{(1)}x + b^{(1)}\big), \quad \ldots, \quad \hat{y} = W^{(L)}h^{(L-1)} + b^{(L)}, \tag{10}$$

with nonlinear activation $\phi(\cdot)$ (e.g., ReLU). Parameters $\Theta = \{W^{(\ell)}, b^{(\ell)}\}$ were optimized by minimizing a supervised loss (e.g., MSE) with early stopping and weight decay. While MLP models are treated as black boxes, interpreting their learned relationships requires post-hoc explanation. We used SHapley Additive exPlanations (SHAP), a Shapley-value based framework, to quantify feature importance by attributing each wavelength's contribution to model predictions under feature coalitions (Lundberg and Lee, 2017).

3.6. Explainable boosting machine (EBM)

We used EBM to obtain an interpretable generalized additive model with boosted shape functions and selected pairwise interactions:

$$\hat{y} = \beta_0 + \sum_{j=1}^{p} g_j(x_j) + \sum_{(j,k)\in I} g_{jk}(x_j, x_k), \tag{11}$$

where g_j and g_{jk} are shallow, boosted trees fit stage-wise (Nori et al., 2019). Because EBM is a glass-box model, it does not require post-hoc explanation; predictions are decomposed into additive, interpretable univariate terms and low-order interactions. We quantify wavelength relevance using EBM's feature importance, derived from the magnitude of each term's contribution across the dataset.

3.7. Experimental study

Stratified random sampling was used to generate 100 independent 70%/30% training and testing splits to ensure comparable representation of lodging condition in model development and evaluation. Stratification was performed by lodging class (Healthy, M-lodged, S-lodged), such that each split preserved the class proportions observed in the full dataset for both ASD and EnMAP. For each split, all models were trained on the 70% training subset and evaluated on the held out 30% testing subset. Performance was summarized across runs using three regression metrics, coefficient of determination (R^2), root mean square error ($\varepsilon_{\mathrm{rmse}}$), and mean absolute error ($\varepsilon_{\mathrm{mae}}$). Algorithm-specific hyperparameters were tuned via Bayesian optimization to identify near-optimal configurations (Akiba et al., 2019). In the PCA–GPR pipeline, we retained three principal components (PCs) for both ASD and EnMAP (Figs. 5(a)–5(b)). Although PC1 explained the majority of variance, PCs 2–3 captured additional, orthogonal spectral variability that improved predictive performance and stability across splits, and together the retained PCs explained ≈ 99% of the cumulative variance. For PLSR, six latent components (LCs) were used for ASD (Fig. 5(c)) and three for EnMAP (Fig. 5(d)), selected based on the performance profiles. The hyperparameter search spaces and bounds for all learning algorithms are summarized in Table 2.

4. Results

4.1. Spectral feature behavior

The spectral analysis illustrated in Fig. 6 aims to distinguish between healthy, moderately lodged, and severely lodged wheat conditions. Fig. 6(a) presents the continuum-removed reflectance spectra for each lodging class across the specified wavelength range. This method emphasizes diagnostic absorption features and spectral transitions in the VIS–NIR–SWIR domains. In the visible to red-edge transition (~670–740 nm), chlorophyll-related absorption in the red (around 670–690 nm) and the red-edge slope are preserved, but separation

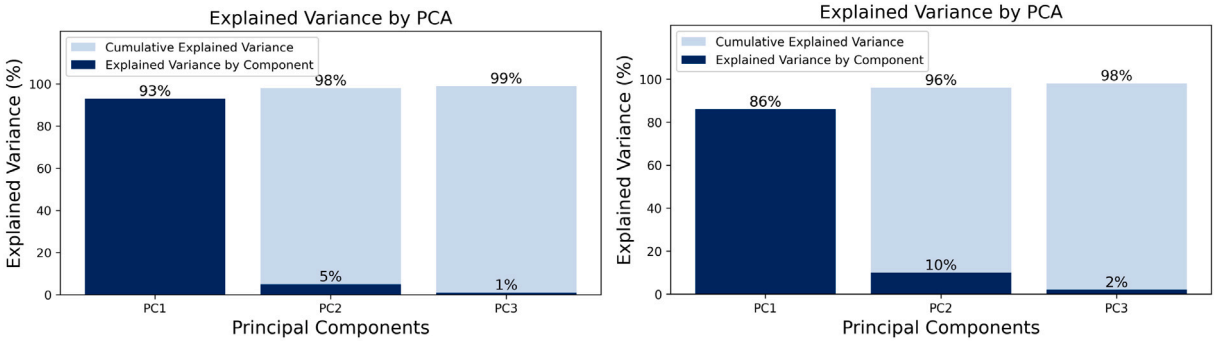

(a) Explained variance ratio (ASD)

(b) Explained variance ratio (EnMAP)

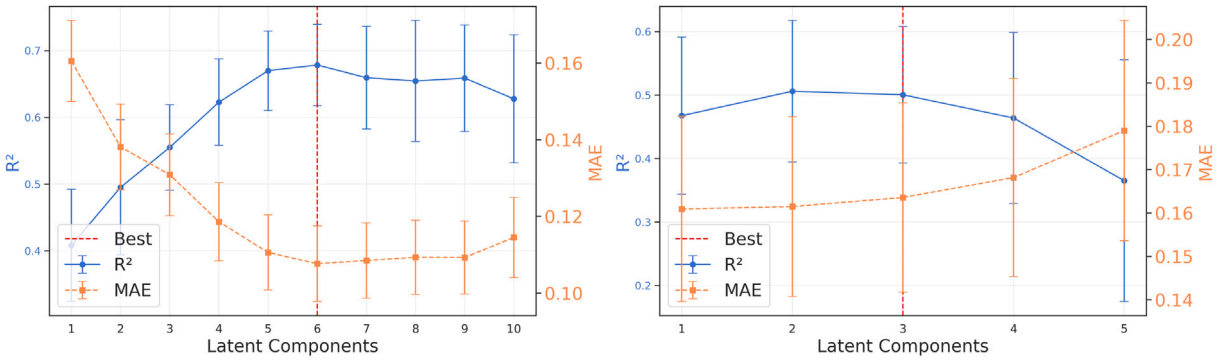

(c) PLSR: model performance vs. LCs (ASD).

(d) PLSR: model performance vs. LCs (EnMAP).

Fig. 5. (a–b) PCA explained-variance profiles for ASD and EnMAP. In both cases, the first three PCs – used in the PCA–GPR pipeline – capture ≈ 99% of the variance. (c–d) PLSR model behavior as a function of the number of latent components, with six LCs used for ASD and three for EnMAP.

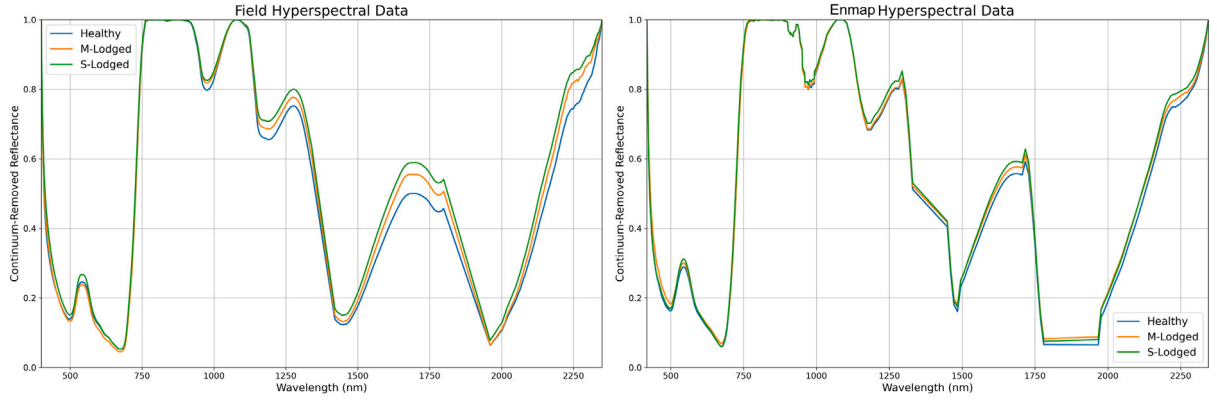

(a) ASD field continuum-removed spectra by lodging class.

(b) EnMAP continuum-removed spectra by lodging class.

Fig. 6. Continuum-removed reflectance from field ASD and EnMAP hyperspectral data for three lodging levels. Both datasets show comparable absorption features and broadly consistent class-dependent differences across wavelength regions, although separation varies by spectral domain in EnMAP due to coarser spectral resolution.

among lodging classes is modest, with considerable overlap across healthy, moderately lodged, and severely lodged spectra (Fig. 6). Clearer contrasts emerge beyond the red-edge, with separations also evident around ~1000 nm and ~1200–1300 nm, and in the SWIR domains at ~1600–1750 nm and ~2100–2250 nm (Fig. 6). When compared with EnMAP continuum-removed reflectance (Fig. 6(b)), the same patterns are preserved but appear smoother and less distinct due to EnMAP's coarser spectral resolution and pixel-scale mixing.

4.2. Performance of TBVI

The wavelength pairs most predictive of LS were identified by computing Pearson correlations for all two-band $TBVI$ combinations (Fig. 7). The maximum absolute correlation was higher for ASD field spectra ($|r| = 0.56$; $n = 189$) than for EnMAP spectra ($|r| = 0.43$; $n = 64$), indicating stronger sensitivity in the denser field measurements. The strongest correlation structures concentrate in interactions between the red-edge (approximately 705–771 nm) and the NIR (about 845–944 nm), and in combinations linking NIR/red-edge bands with SWIR domains (around 1590–1740 nm and 2120–2345 nm) that are sensitive to canopy water content and dry-matter/biochemical absorption. Importantly, the heatmaps show both positive and negative correlation regimes, and several wavelength-pair regions exhibit sign changes between ASD and EnMAP, reflecting scale differences, coarser spectral sampling, and residual atmospheric and adjacency effects in satellite reflectance. Collectively, these patterns indicate that a limited set of wavelength regions

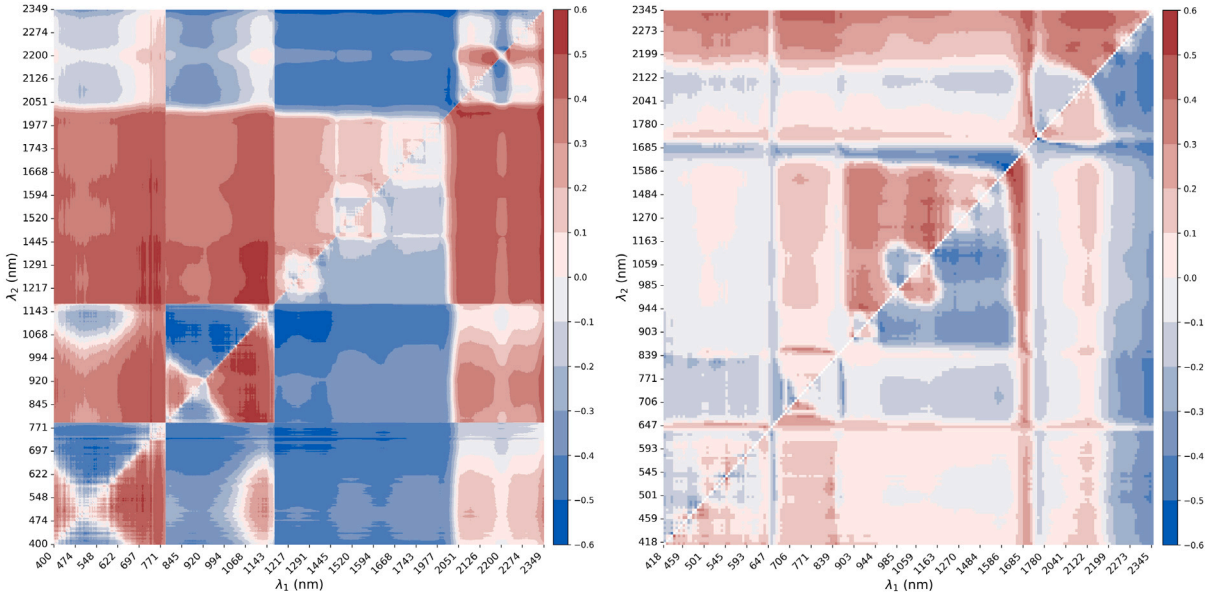

(a) ASD $TBVI$ heatmap (b) EnMAP $TBVI$ heatmap

Fig. 7. Heatmaps of Pearson correlation coefficients between TBVIs and LS derived from (a) ASD field spectra (n = 189) and (b) EnMAP spectra (n = 64). Blue denotes negative correlations and red positive correlations, indicating where TBVI is inversely or positively related to LS.

Table 3
Mean vs. best-fold accuracy metrics for each regression strategy for the prediction of LS, based on ASD and EnMAP derived spectra.

Data source	Method	$\text{Accuracy}_{\text{mean}}$			$\text{Accuracy}_{\text{best}}$		
		ϵ_{mae}	ϵ_{rmse}	R^2	ϵ_{mae}	ϵ_{rmse}	R^2
ASD	PCA-GPR	0.11 ± 0.02	0.15 ± 0.02	0.65 ± 0.10	0.08	0.11	0.80
	PLSR	0.12 ± 0.02	0.16 ± 0.02	0.58 ± 0.12	0.08	0.10	0.80
	MLP	0.11 ± 0.02	0.15 ± 0.02	0.65 ± 0.10	0.08	0.11	0.82
	EBM	0.11 ± 0.01	0.15 ± 0.02	0.66 ± 0.07	0.07	0.10	0.84
EnMAP	PCA-GPR	0.14 ± 0.02	0.20 ± 0.03	0.48 ± 0.15	0.10	0.12	0.74
	PLSR	0.17 ± 0.02	0.20 ± 0.03	0.46 ± 0.15	0.09	0.13	0.77
	MLP	0.14 ± 0.03	0.18 ± 0.03	0.58 ± 0.14	0.09	0.11	0.78
	EBM	0.14 ± 0.02	0.18 ± 0.02	0.60 ± 0.08	0.08	0.11	0.78

centered on 550, 670, 720–740, 865, 1650, and 2130–2190 nm captures much of the discriminatory power for detecting and quantifying wheat lodging.

4.3. Machine–learning model accuracy

Table 3 compares the performance of the ML models for predicting LS using ASD field spectra (n = 189) and EnMAP spectra (n = 64), reported with ϵ_{mae}, ϵ_{rmse}, and R^2. Across all four algorithms, models trained on ASD field spectra consistently outperformed those trained on EnMAP inputs for predicting LS. This difference is consistent with several factors, including the larger number of ASD observations and the finer spectral sampling and more controlled measurement geometry of field spectroscopy, which together can improve model calibration and reduce variance under repeated train–test splits.

The ASD models achieved lower errors and higher explained variance than their EnMAP counterparts. For ASD, the mean ϵ_{RMSE} was $\sim$ 0.15–0.16 and mean R^2 $\sim$ 0.58–0.66. For EnMAP, mean RMSE was $\sim$ 0.18–0.20 and mean R^2 $\sim$ 0.46–0.60. On ASD, EBM achieved the strongest mean performance (R^2 = 0.66 ± 0.07; ϵ_{MAE} = 0.11 ± 0.01; ϵ_{RMSE} = 0.15 ± 0.02), closely followed by MLP and PCA-GPR (both $R^2 \approx 0.65$). PLSR trailed slightly (R^2 = 0.58 ± 0.12). On EnMAP, EBM and MLP tied on error (both mean RMSE $\approx$ 0.18) and led in explained variance (R^2 = 0.60±0.08 and 0.58±0.14, respectively), while PCA-GPR and PLSR performed moderately ($R^2 \approx$ 0.46–0.48; RMSE $\approx$ 0.20).

Scatter plots of predicted vs. measured LS Figs. 8 mirror the metrics given in Table 3. For ASD, points cluster tightly along the 1:1 line, most clearly for EBM and MLP, indicating low bias and reduced spread across the LS range. EnMAP predictions show slightly wider dispersion, especially at mid-to-high LS, yet EBM and MLP again produce the most compact clouds among the EnMAP models. Visual inspection also suggests fewer extreme under- and over- estimations for ASD than for EnMAP.

The higher performance obtained with ASD is consistent with its denser spectral sampling and more controlled observation geometry, which better preserve subtle absorption features and continuum-shape differences associated with lodging. The competitive performance of EnMAP, particularly with EBM and MLP, indicates that satellite hyperspectral observations retain sufficient information for lodging mapping despite coarser spectral resolution and pixel-scale mixing. In practice, field spectroscopy represents an upper bound on achievable accuracy, while EnMAP provides a scalable satellite-based basis for lodging assessment when cloud-free acquisitions are available.

4.4. Identifying informative wavelengths for ML models

We identified informative wavelength regions for lodging severity prediction using complementary, model-specific interpretability outputs. Specifically, we inspected PCA loadings from the PCA–GPR pipeline to characterize dominant modes of spectral variability, VIP scores from PLSR to summarize response relevant wavelengths, global SHAP importance from the MLP to quantify nonlinear wavelength contributions, and EBM feature importance to assess additive wavelength

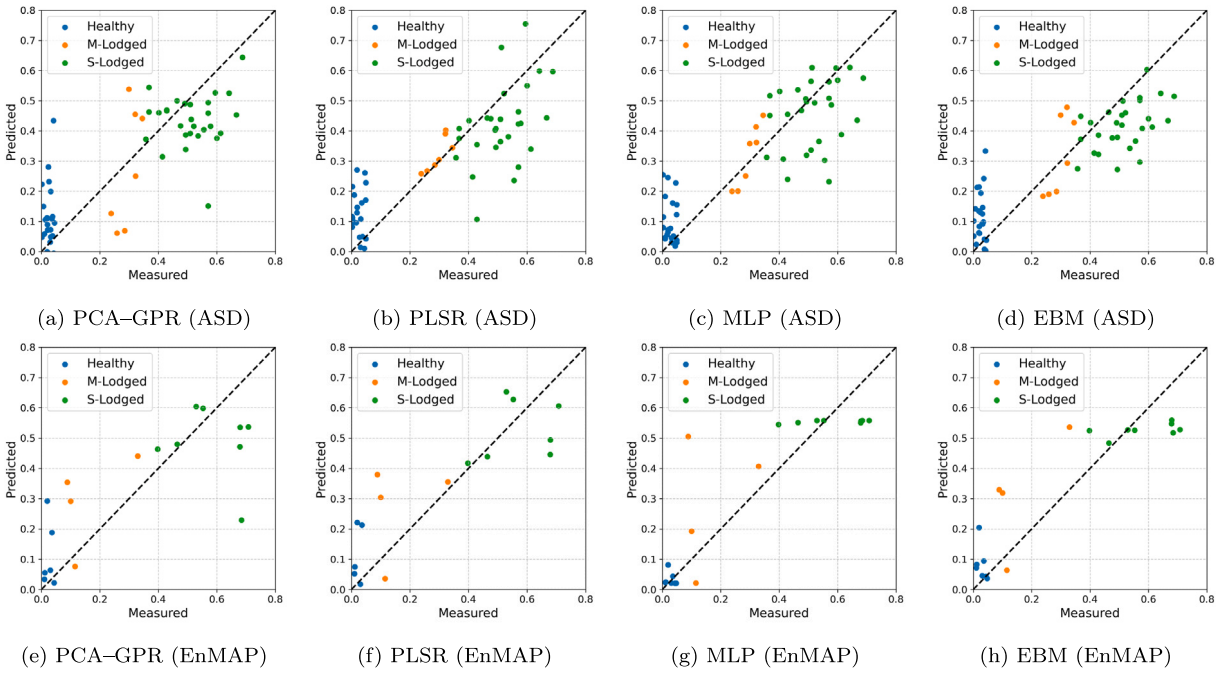

(a) PCA–GPR (ASD) (b) PLSR (ASD) (c) MLP (ASD) (d) EBM (ASD)

(e) PCA–GPR (EnMAP) (f) PLSR (EnMAP) (g) MLP (EnMAP) (h) EBM (EnMAP)

Fig. 8. Scatter plots of predicted vs. measured LS for four ML models (a–e) PCA–GPR, (b–f) PLSR, (c–g) MLP, and (d–h) EBM, shown for the best-performing split (highest test R^2) for each model and data source. Points are color-coded by lodging class: Healthy, M-lodged, and S-lodged.

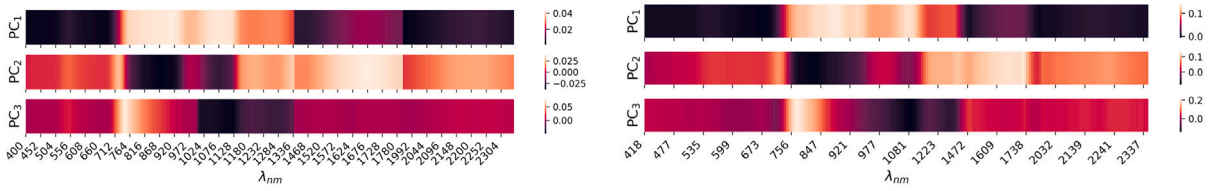

(a) ASD spectra: loadings of the first three PCs across wavelengths. Peaks denote influential spectral regions.

(b) EnMAP reflectance: loadings of the first three PCs across wavelengths, showing similar dominant regions as (a).

Fig. 9. PCA loadings for field-based (ASD) and image-based (EnMAP) spectra. For each dataset, the leading PCs isolate wavelength regions that explain the largest fractions of input variance.

effects. For each approach, we compared the dominant peaks between ASD and EnMAP to evaluate the degree of overlap in informative spectral domains across sensors.

PCA loadings (PCA–GPR) Loading patterns of the leading PCs (Figs. 9(a) and 9(b)) highlight wavelength regions that most strongly shape each component and, therefore, the spectral domains that dominate variability in the inputs (Fig. 9).

VIP scores (PLSR) VIP profiles derived from the PLSR models (Fig. 10) highlight wavelength regions that contribute most strongly to lodging severity prediction. Wavelengths with VIP > 1 are commonly interpreted as response-relevant, while the relative height and width of VIP peaks provide additional information on the dominance and spectral extent of informative regions, supporting comparison between ASD and EnMAP.

SHAP importance (MLP) Global SHAP importance curves for the MLP models (Fig. 11) summarize wavelength relevance using mean absolute SHAP values across samples, where larger values indicate greater overall influence on MLP predictions. Dominant peaks were compared between ASD and EnMAP to assess cross-sensor consistency.

EBM feature importance EBM feature-importance profiles (Fig. 12) highlight wavelength regions that contribute most strongly to lodging score (LS) prediction. Dominant peaks were compared between ASD and EnMAP to evaluate the consistency of informative spectral domains across sensors.

5. Discussion

This study demonstrates that hyperspectral remote sensing can support wheat lodging assessment at both field and satellite scales and that ASD and EnMAP share partially overlapping spectral response patterns associated with lodging related canopy alteration. The analysis of key wavelength regions across models and interpretability frameworks provided converging evidence that lodging sensitivity is concentrated in the visible, red-edge/NIR, and SWIR domains, linking structural canopy changes to a compact set of informative spectral regions.

The spectral behavior of both ASD and EnMAP showed that lodging altered the canopy's spectral response, influencing several key absorption features (Fig. 6). In the visible-red to red-edge transition (~670–740 nm), chlorophyll-related absorption in the red (around 670–690 nm) and the red-edge slope are preserved in both sensors, but class separation is modest in the continuum-removed profiles, with considerable overlap among healthy, moderately lodged, and severely lodged wheat (Fig. 6). Clearer contrasts emerge beyond the red-edge, with separations also evident around ~1000 nm and ~1200–1300 nm, and in the SWIR domains at ~1600–1750 nm and ~2100–2250 nm (Fig. 6). When comparing this behavior with EnMAP continuum-removed reflectance, the same trends were observed but appeared smoother and less distinct due to the sensor's coarser spectral resolution relative to the ASD measurements.

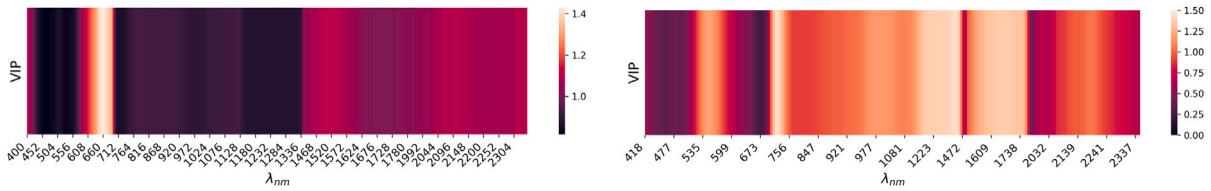

(a) ASD spectra: VIP scores across wavelengths. The horizontal line at VIP = 1 marks the common importance threshold.

(b) EnMAP reflectance: VIP scores across wavelengths, highlighting response-relevant regions similar to (a).

Fig. 10. PLSR-based Variable Importance in Projection (VIP) for (a) ASD field spectra and (b) EnMAP reflectance. Peaks indicate wavelengths with high response relevance after accounting for component weighting.

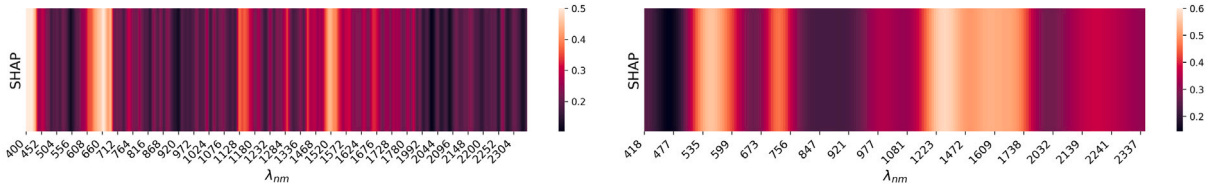

(a) ASD spectra: global importance from the absolute mean SHAP values

(b) EnMAP reflectance: SHAP-based importance across wavelengths, analogous to (a).

Fig. 11. Global feature importance derived from the absolute mean SHAP values for MLP models trained on (a) ASD and (b) EnMAP spectra ; higher values denote larger performance contributions.

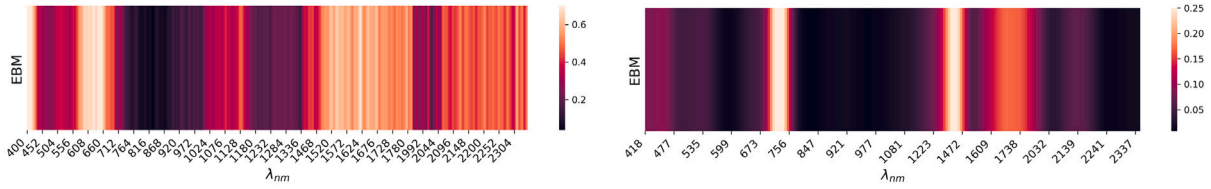

(a) ASD spectra: EBM feature importance summarizing additive contributions across wavelengths.

(b) EnMAP reflectance: EBM feature importance across wavelengths, comparable to (a).

Fig. 12. Wavelength-resolved EBM feature importance for (a) ASD field spectra and (b) EnMAP reflectance, shown across the full hyperspectral domain.

Among the tested learning algorithms, EBM and MLP provided the highest predictive accuracy for both ASD and EnMAP, suggesting that nonlinear modeling is beneficial for capturing the LS–reflectance relationship. The lower accuracy obtained with EnMAP relative to ASD can be attributed to three main factors. First, ASD provides finer spectral sampling, which better preserves narrow absorption features and subtle continuum-shape differences associated with lodging. Second, ASD measurements represent a smaller instantaneous field of view and a more controlled observation geometry, reducing within sample heterogeneity compared with satellite pixels that integrate variability across larger areas. Third, ASD reflectance is subject to negligible atmospheric effects relative to spaceborne observations; despite the use of atmospherically corrected Level-2 A products, residual atmospheric and adjacency effects can still reduce spectral contrast in EnMAP data. In addition, the ASD dataset contained more observations, which can improve model calibration and reduce variance under repeated train–test splits.

Part of the ASD–EnMAP performance difference may also arise from differences in observation geometry. ASD spectra were collected under controlled near-nadir conditions, whereas EnMAP reflectance is influenced by solar and viewing geometry at the time of acquisition. These BRDF-related differences were not explicitly normalized in the present analysis and may contribute to cross-sensor discrepancies alongside spectral resolution, sample size, and mixed-pixel effects.

While hyperspectral imagery provides both spectral and spatial information, our EnMAP analysis was based on plot-level spectra obtained by averaging a 3 × 3 pixel window and therefore did not explicitly incorporate spatial descriptors such as texture, edge structure, or neighborhood statistics that may better characterize lodging patterns. This design choice was made to preserve spectral interpretability and maintain consistency with the ASD-based analysis, but it likely reduced sensitivity to heterogeneous lodging conditions within 30 m pixels. Future work could extend this framework by incorporating either spatial information, for example through texture measures or patch-based deep learning models, or more advanced spectral deep learning approaches, such as one-dimensional convolutional networks that learn diagnostic spectral patterns directly from hyperspectral signals. This may partly explain why EnMAP-based predictions were less accurate than ASD-based predictions, as ASD measurements were more directly linked to the sampled microplots and less affected by mixed-pixel variability, whereas EnMAP pixels integrate a broader range of ground conditions at the 30 m scale. The performance difference is also attributable to coarser spectral sampling, smaller sample size, and within-pixel heterogeneity in the satellite data.

Across the interpretability analyses, six spectral domains repeatedly emerged as influential for lodging detection using hyperspectral remote sensing, and these spectral regions have also been reported in other crop lodging studies. The significance of the visible region (550–680 nm) showed by the VIP and SHAP importance tests corresponds well with findings from wheat, maize, and rice lodging studies using multispectral and hyperspectral remote sensing, where reductions in chlorophyll content shown to be early spectral indicators of lodging (Guan et al., 2022; Chen et al., 2022). PCA and VIP analyses identified pronounced contributions around 720–740 nm, corresponding to the red-edge inflection point, reinforcing its sensitivity to lodging

due to reductions in chlorophyll content and aligning with UAV- and MSI-based lodging assessments (Guan et al., 2022; Chauhan et al., 2020c). Similarly, both SHAP and EBM highlighted the importance of the NIR region around 850–880 nm, which reflects canopy structural collapse, a pattern observed in wheat and maize lodging studies (Chauhan et al., 2020c; Qu et al., 2023; Sun et al., 2022). Furthermore, VIP, SHAP, and EBM analyses showed strong importance in two SWIR regions (1600–1750 nm and 2100–2220 nm), which is consistent with reported lodging-induced changes in water content and dry matter composition in wheat and rice (Chauhan et al., 2020c; Wang et al., 2020). Altogether, these results reinforce that the red-edge-NIR-SWIR spectral regions capture the key physiological and structural responses to lodging and reflect lodging signatures broadly observed across multiple crops and sensors. Collectively, these domains overlap with the high-correlation TBVI regions (550, 670, 720–740, 865, 1650, and 2130–2190 nm) identified earlier (Fig. 7), indicating that both narrowband and model-based analyses highlight broadly similar wavelength domains associated with lodging. In particular, the red-edge–NIR–SWIR continuum emerged as a broadly consistent and biophysically meaningful wavelength domain for distinguishing lodging severity.

The identified wavelength domains should also be interpreted with caution because lodged canopies may alter the observed signal through multiple mechanisms. Under nadir-viewing conditions and at severe lodging levels, increased visibility of soil and shaded background may contribute to the measured reflectance. At the same time, lodging also changes canopy architecture itself, including leaf and stem orientation, the relative visibility of different plant tissues, and the internal scattering behavior of the canopy. In dense wheat canopies, these structural and radiative effects may be as important as, or more important than, background exposure. In the present study, fractional vegetation cover and soil-exclusion thresholds were not explicitly quantified, and canopy and background components were not separated. Our findings indicate that, in the dense wheat canopies examined in this study, the soil background was not visually apparent based on field observation, suggesting that its contribution to the measured reflectance was likely minimal. The observed spectral–lodging relationships should therefore be interpreted mainly as integrated responses to lodging-induced canopy reorganization rather than as soil-driven signals.

The complementary nature of the interpretability approaches enhances confidence in the identified spectral drivers. PCA loadings primarily captured data variance, emphasizing structural wavelengths independent of response variables. In contrast, VIP provided supervised insight, weighting wavelengths by their explanatory power for lodging severity. SHAP further disentangled nonlinear dependencies learned by MLP, revealing overlapping peaks at the red-edge and SWIR regions, while EBM yielded smooth, interpretable additive feature curves, confirming similar trends but with clearer physiological separation. Together, these methods indicate that both pigment-related (visible-red-edge) and structural-biochemical (NIR–SWIR) domains jointly determine lodging reflectance signatures.

The partially overlapping spectral patterns across ASD and EnMAP indicate that field-to-satellite transfer of informative wavelength domains is feasible for wheat lodging assessment under cloud-free conditions, but this study does not demonstrate temporal monitoring or broad operational deployment because only a single EnMAP acquisition was analyzed at one study site. EnMAP's revisit cycle and cloud constraints limit its use as a standalone operational monitoring source; however, hyperspectral acquisitions can still provide biophysically specific calibration and interpretation that complements higher temporal sensors such as multispectral and SAR time series. While full-range field spectroscopy provides detailed diagnostic power, EnMAP's spectral coverage captures the red-edge and SWIR absorption features that are relevant for lodging-related structural and moisture changes. For future hyperspectral missions and observing strategies, narrow spectral sensitivity around ~720, 860, 1650, and 2130 nm would support discrimination of pigment, structure, and dry-matter and water-related effects, especially when integrated with more frequent observations from other sensors.

This study is based on a single EnMAP acquisition and one field campaign period and therefore does not evaluate the temporal development of lodging. The results should be interpreted as a single-time assessment of lodging severity rather than a temporal monitoring framework. Multi temporal hyperspectral observations, whether from repeated field spectroscopy or future spaceborne acquisitions, would help determine how stable the identified wavelength domains remain before, during, and after lodging events. From a longer-term perspective, future spaceborne hyperspectral missions such as CHIME, planned as a two satellite constellation with expected revisiting time of 11 days (European Space Agency, 2026), may improve the availability of hyperspectral observations for crop monitoring, particularly when combined with higher-temporal multispectral or SAR data.

A limitation of this study is that it was conducted within a single commercial farm in northern Italy and therefore does not test transferability across broader environmental, management, and cultivar conditions. Although the study area included multiple wheat parcels and three wheat types, the reported model performance should be interpreted as site-specific evidence of feasibility rather than as proof of generalizability for operational deployment. Future work should evaluate model stability across multiple farms, seasons, soil backgrounds, and wheat varieties.

The inclusion of three wheat types (emmer, durum and soft wheat) may also have introduced cultivar dependent spectral variability, since differences in canopy architecture, plant height, phenology, and biochemical composition can affect both baseline reflectance and lodging response. Cultivar was not treated as an explicit covariate in the present analysis, and cultivar-stratified modeling was not performed. The reported relationships should therefore be interpreted at the study-site level rather than as cultivar specific calibrations. At the same time, the ability to detect lodging-related spectral responses across the sampled wheat types suggests that hyperspectral observations retain sensitivity to structural changes associated with lodging, even though cultivar effects were not explicitly separated. Future work should test whether lodging-sensitive wavelength domains remain stable across wheat varieties and whether cultivar-aware modeling improves transferability and operational robustness.

6. Conclusion

This study shows that hyperspectral data, acquired from field ASD measurements and from a single EnMAP acquisition, can support wheat lodging severity estimation under the study conditions. By combining spectral preprocessing, two-band vegetation indices, and multiple machine-learning models with complementary interpretability analyses, we identified wavelength domains repeatedly associated with lodging-induced canopy change. Across methods, the most informative regions were concentrated around 550, 670, 720–740, 865, 1650, and 2130–2190 nm. Field ASD spectra yielded higher predictive accuracy than EnMAP data, consistent with denser spectral sampling and more controlled acquisition geometry. The overlap in identified wavelength domains suggests that field-derived hyperspectral diagnostics can inform satellite-based analyses, while acknowledging remaining limitations related to scale mismatch, observation geometry, and single-site validation.

These findings highlight the potential of hyperspectral imaging and interpretable ML models to support lodging severity assessment in satellite-based workflows, particularly as a calibration and interpretation layer alongside higher-temporal multispectral and SAR observations. As a proof-of-concept study, this work demonstrates the feasibility of hyperspectral lodging assessment under the conditions examined. Future hyperspectral missions and sensor designs may benefit from preserving sensitivity in the identified wavelength regions, while further evaluation across multiple sites, seasons, and cereal types would strengthen the broader applicability of this framework.

CRediT authorship contribution statement

Mehmet Furkan Celik: Writing – original draft, Visualization, Validation, Software, Methodology, Investigation, Formal analysis, Data curation, Conceptualization. **Padmageetha Nagarajan:** Writing – review & editing, Investigation, Data curation, Conceptualization. **Andrew Nelson:** Writing – review & editing, Supervision, Project administration, Methodology, Funding acquisition, Conceptualization. **Zaib Unnisa:** Writing – review & editing, Conceptualization. **Booker Ogutu:** Writing – review & editing, Conceptualization. **Jadunandan Dash:** Writing – review & editing, Conceptualization. **Mirco Boschetti:** Writing – review & editing, Conceptualization. **Ewelina Dobrowolska:** Writing – review & editing, Conceptualization. **Espen Volden:** Writing – review & editing, Conceptualization. **Roshanak Darvishzadeh:** Writing – review & editing, Supervision, Resources, Project administration, Methodology, Funding acquisition, Conceptualization.

Declaration of competing interest

The authors declare that they have no known competing financial interests or personal relationships that could have appeared to influence the work reported in this paper.

Acknowledgments

This research was partly supported by the EO4CerealStress project, monitoring crop response to multiple stressors (ESA AO/1-11144/22/I-EF), funded by the European Space Agency (ESA) under Agricultural Science Precursors – EXPRO+ (Theme 3). Dr. Roshanak Darvishzadeh also acknowledges support from the Netherlands Organisation for Scientific Research (NWO) through her NL-CGIAR Senior Expert Grant.

Data availability

EnMAP Level-2A imagery was obtained under the EnMAP data access framework and may be subject to licensing and redistribution constraints. Measured plot-level spectra, lodging parameters, and code used for analysis can be made available by the corresponding author upon reasonable request, subject to data-sharing agreements and institutional policies.

References

Akiba, T., Sano, S., Yanase, T., Ohta, T., Koyama, M., 2019. Optuna: A next-generation hyperparameter optimization framework. In: Proc. 25th ACM SIGKDD Int. Conf. Knowl. Discov. Data Min.. pp. 2623–2631. http://dx.doi.org/10.48550/arXiv.1907.10902.

Ali, N., Mohammed, A., Bais, A., Sangha, J.S., Ruan, Y., Cuthbert, R.D., 2023. LodgeNet: An automated framework for precise detection and classification of wheat lodging severity levels in precision farming. Front. Plant Sci. 14, 1255961. http://dx.doi.org/10.3389/fpls.2023.1255961.

Azizi, A., Zhang, Z., Rui, Z., Li, Y., Igathinathane, C., Flores, P., Mathew, J., Pourreza, A., Han, X., Zhang, M., 2024. Comprehensive wheat lodging detection after initial lodging using UAV RGB images. Expert Syst. Appl. 238, 121788. http://dx.doi.org/10.1016/j.eswa.2023.121788.

Baker, C.J., 1995. The development of a theoretical model for the windthrow of plants. J. Theoret. Biol. 175 (3), 355–372. http://dx.doi.org/10.1006/jtbi.1995.0147.

Baker, C.J., Berry, P.M., Spink, J.H., Sylvester-Bradley, R., Griffin, J.M., Scott, R.K., Clare, R.W., 1998. A method for the assessment of the risk of wheat lodging. J. Theoret. Biol. 194 (4), 587–603. http://dx.doi.org/10.1006/jtbi.1998.0778.

Baker, C.J., Sterling, M., Berry, P., 2014. A generalised model of crop lodging. J. Theoret. Biol. 363, 1–12. http://dx.doi.org/10.1016/j.jtbi.2014.07.032.

Berry, P.M., Spink, J., 2012. Predicting yield losses caused by lodging in wheat. Field Crop. Res. 137, 19–26. http://dx.doi.org/10.1016/j.fcr.2012.07.019.

Celik, M.F., Isik, M.S., Taskin, G., Erten, E., Camps-Valls, G., 2023. Explainable artificial intelligence for cotton yield prediction with multisource data. IEEE Geosci. Remote. Sens. Lett. 20, 1–5. http://dx.doi.org/10.1109/LGRS.2023.3303643.

Chapman, S.C., Merz, T., Chan, A., Jackway, P., Hrabar, S., Dreccer, M.F., Holland, E., Zheng, B., Ling, T.J., Jimenez-Berni, J., 2014. Pheno-Copter: A low-altitude, autonomous remote-sensing robotic helicopter for high-throughput field-based phenotyping. Agronomy 4 (2), 279–301. http://dx.doi.org/10.3390/agronomy4020279.

Chauhan, S., Darvishzadeh, R., Boschetti, M., Nelson, A., 2020a. Discriminant analysis for lodging severity classification in wheat using RADARSAT-2 and Sentinel-1 data. ISPRS J. Photogramm. Remote Sens. 164, 138–151. http://dx.doi.org/10.1016/j.isprsjprs.2020.04.012.

Chauhan, S., Darvishzadeh, R., Boschetti, M., Nelson, A., 2020b. Estimation of crop angle of inclination for lodged wheat using multi-sensor SAR data. Remote Sens. Environ. 236, 111488. http://dx.doi.org/10.1016/j.rse.2019.111488.

Chauhan, S., Darvishzadeh, R., Boschetti, M., Pepe, M., Nelson, A., 2019. Remote sensing-based crop lodging assessment: Current status and perspectives. ISPRS J. Photogramm. Remote Sens. 151, 124–140. http://dx.doi.org/10.1016/j.isprsjprs.2019.03.005.

Chauhan, S., Darvishzadeh, R., van Delden, S.H., Boschetti, M., Nelson, A., 2021. Mapping of wheat lodging susceptibility with synthetic aperture radar data. Remote Sens. Environ. 259, 112427. http://dx.doi.org/10.1016/j.rse.2021.112427.

Chauhan, S., Darvishzadeh, R., Lu, Y., Boschetti, M., Nelson, A., 2020c. Understanding wheat lodging using multi-temporal Sentinel-1 and Sentinel-2 data. Remote Sens. Environ. 243, 111804. http://dx.doi.org/10.1016/j.rse.2020.111804.

Chen, Y., Sun, L., Pei, Z., Sun, J., Li, H., Jiao, W., You, J., 2022. A simple and robust spectral index for identifying lodged maize using Gaofen-1 satellite data. Sensors 22 (3), 989. http://dx.doi.org/10.3390/s22030989.

Dai, X., Chen, S., Jia, K., Jiang, H., Sun, Y., Li, D., Zheng, Q., Huang, J., 2022. A decision-tree approach to identifying paddy rice lodging with multiple pieces of polarization information derived from Sentinel-1. Remote. Sens. 15 (1), 240. http://dx.doi.org/10.3390/rs15010240.

Darvishzadeh, R., 2025. Monitoring vegetation stress and health disturbances: A remote sensing perspective. Arab Near East Plant Prot. Bull. 96, 4–6, URL https://asplantprotection.org/en/issue-96-december-2025/. (Accessed 09 January 2026).

Darvishzadeh, R., Skidmore, A., Atzberger, C., van Wieren, S., 2008. Estimation of vegetation LAI from hyperspectral reflectance data: Effects of soil type and plant architecture. Int. J. Appl. Earth Obs. Geoinf. 10 (3), 358–373. http://dx.doi.org/10.1016/j.jag.2008.02.005.

European Space Agency, 2026. CHIME (Copernicus Hyperspectral Imaging Mission for the Environment). URL https://www.eoportal.org/satellite-missions/chime-copernicus#eop-quick-facts-section. (Accessed 19 March 2026).

FAO, 2024. Agricultural production statistics 2010–2023. Technical Report FAOSTAT Analytical Brief No. 96, Food and Agriculture Organization of the United Nations (FAO), Rome, ISSN 2709-006X (Print), ISSN 2709-0078 (Online). Licence: CC-BY-4.0. URL https://openknowledge.fao.org/items/ab36b259-d641-4ded-8832-32f579685be7.

Guan, H., Huang, J., Li, X., Zeng, Y., Su, W., Ma, Y., Dong, J., Niu, Q., Wang, W., 2022. An improved approach to estimating crop lodging percentage with Sentinel-2 imagery using machine learning. Int. J. Appl. Earth Obs. Geoinf. 113, 102992. http://dx.doi.org/10.1016/j.jag.2022.102992.

Guo, R., Zhu, X., Liu, T., 2023. Automatic detection of crop lodging from multitemporal satellite data based on the isolation forest algorithm. Comput. Electron. Agric. 215, 108415. http://dx.doi.org/10.1016/j.compag.2023.108415.

Han, D., Yang, H., Yang, G., Qiu, C., 2017. Monitoring model of corn lodging based on sentinel-1 radar image. In: 2017 SAR in Big Data Era: Models, Methods and Applications (BIGSARDATA). pp. 1–5. http://dx.doi.org/10.1109/BIGSARDATA.2017.8124928.

Jiang, S., Hao, J., Li, H., Zuo, C., Geng, X., Sun, X., 2022. Monitoring wheat lodging at various growth stages. Sensors 22 (18), 6967. http://dx.doi.org/10.3390/s22186967.

Jolliffe, I.T., Cadima, J., 2016. Principal component analysis: A review and recent developments. Philos. Trans. R. Soc. A 374 (2065), 20150202. http://dx.doi.org/10.1098/rsta.2015.0202.

Kokaly, R.F., Clark, R.N., 1999. Spectroscopic determination of leaf biochemistry using band-depth analysis of absorption features and stepwise multiple linear regression. Remote Sens. Environ. 67 (3), 267–287. http://dx.doi.org/10.1016/S0034-4257(98)00084-4.

Liu, Z., Li, C., Wang, Y., Huang, W., Ding, X., Zhou, B., Wu, H., Wang, D., Shi, J., 2011. Comparison of spectral indices and principal component analysis for differentiating lodged rice crop from normal ones. In: Int. Conf. Comput. Comput. Technol. Agric.. pp. 84–92. http://dx.doi.org/10.1007/978-3-642-27278-3_10.

Liu, H.Y., Yang, G.J., Zhu, H.C., 2014. The extraction of wheat lodging area in UAV images using spectral and texture features. Appl. Mech. Mater. 651, 2390–2393. http://dx.doi.org/10.4028/www.scientific.net/AMM.651-653.2390.

Lundberg, S.M., Lee, S.-I., 2017. A unified approach to interpreting model predictions. Adv. Neural Inf. Process. Syst. 30, http://dx.doi.org/10.48550/arXiv.1705.07874.

Murakami, T., Yui, M., Amaha, K., 2012. Canopy height measurement by photogrammetric analysis of aerial images: Application to buckwheat (Fagopyrum esculentum moench) lodging evaluation. Comput. Electron. Agric. 89, 70–75. http://dx.doi.org/10.1016/j.compag.2012.08.003.

Murtagh, F., 1991. Multilayer perceptrons for classification and regression. Neurocomputing 2 (5–6), 183–197. http://dx.doi.org/10.1016/0925-2312(91)90023-5.

Mutanga, O., Skidmore, A.K., 2004. Narrow band vegetation indices overcome the saturation problem in biomass estimation. Int. J. Remote Sens. 25 (19), 3999–4014. http://dx.doi.org/10.1080/01431160310001654923.

Nori, H., Jenkins, S., Koch, P., Caruana, R., 2019. InterpretML: A unified framework for machine learning interpretability. http://dx.doi.org/10.48550/arXiv.1909.09223.

Pinthus, M.J., 1974. Lodging in wheat, barley, and oats: The phenomenon, its causes, and preventive measures. Adv. Agron. 25, 209–263. http://dx.doi.org/10.1016/S0065-2113(08)60782-8.

Qu, X., Zhou, J., Gu, X., Wang, Y., Sun, Q., Pan, Y., 2023. Monitoring maize lodging severity based on multi-temporal Sentinel-1 images using time-weighted dynamic time warping. Comput. Electron. Agric. 215, 108365. http://dx.doi.org/10.1016/j.compag.2023.108365.

Rajkumara, S., 2008. Lodging in cereals — a review. Agric. Rev. 29 (1), 55–60.

Rosipal, R., Krämer, N., 2005. Overview and recent advances in partial least squares. In: Subspace, Latent Structure and Feature Selection. pp. 34–51. http://dx.doi.org/10.1007/11752790_2.

Sarker, M.M., Mizuno, Y., Ono, K., Kobayashi, T., Nasahara, K.N., 2026. Assessment of spectral indices for detecting rice phenological stages using long-term in situ hyperspectral observations and Sentinel-2 data. AgriEngineering 8 (1), 14. http://dx.doi.org/10.3390/agriengineering8010014.

Sun, Q., Chen, L., Zhang, B., Qu, X., Cui, Y., Shu, M., Gu, X., 2024. Evaluation of growth recovery grade in lodging maize via UAV-based hyperspectral images. J. Remote. Sens. 4, 0253. http://dx.doi.org/10.34133/remotesensing.0253.

Sun, Q., Gu, X., Chen, L., Xu, X., Wei, Z., Pan, Y., Gao, Y., 2022. Monitoring maize canopy chlorophyll density under lodging stress based on UAV hyperspectral imagery. Comput. Electron. Agric. 193, 106671. http://dx.doi.org/10.1016/j.compag.2021.106671.

Tang, Z., Sun, Y., Wan, G., Zhang, K., Shi, H., Zhao, Y., Chen, S., Zhang, X., 2022. Winter wheat lodging area extraction using deep learning with GaoFen-2 satellite imagery. Remote. Sens. 14 (19), 4887. http://dx.doi.org/10.3390/rs14194887.

Wang, J., Li, K., Shao, Y., Zhang, F., Wang, Z., Guo, X., Qin, Y., Liu, X., 2020. Analysis of combining SAR and optical optimal parameters to classify typhoon-invasion lodged rice: A case study using the random forest method. Sensors 20 (24), 7346. http://dx.doi.org/10.3390/s20247346.

Williams, C., Rasmussen, C., 1995. Gaussian processes for regression. Adv. Neural Inf. Process. Syst. 8.

Yang, H., Chen, E., Li, Z., Zhao, C., Yang, G., Pignatti, S., Casa, R., Zhao, L., 2015. Wheat lodging monitoring using polarimetric index from RADARSAT-2 data. Int. J. Appl. Earth Obs. Geoinf. 34, 157–166. http://dx.doi.org/10.1016/j.jag.2014.08.010.

Yang, M.-D., Huang, K.-S., Kuo, Y.-H., Tsai, H.P., Lin, L.-M., 2017. Spatial and spectral hybrid image classification for rice lodging assessment through UAV imagery. Remote. Sens. 9 (6), 583. http://dx.doi.org/10.3390/rs9060583.

Yu, J., Cheng, T., Cai, N., Zhou, X.-G., Diao, Z., Wang, T., Du, S., Liang, D., Zhang, D., 2023. Wheat lodging segmentation based on LSTM_PSPNet deep learning network. Drones 7 (2), 143. http://dx.doi.org/10.3390/drones7020143.

Zang, H., Su, X., Wang, Y., Li, G., Zhang, J., Zheng, G., Hu, W., Shen, H., 2024. Automatic grading evaluation of winter wheat lodging based on deep learning. Front. Plant Sci. 15, 1284861. http://dx.doi.org/10.3389/fpls.2024.1284861.

Zhang, Z., Flores, P., Igathinathane, C., L. Naik, D., Kiran, R., Ransom, J.K., 2020. Wheat lodging detection from UAS imagery using machine learning algorithms. Remote. Sens. 12 (11), http://dx.doi.org/10.3390/rs12111838.

Zhang, B., Shu, M., Bao, X., Dai, M., Sun, Q., Sun, X., Zhang, M., Ren, Y., Li, Z., Tian, Y., et al., 2026. Large-scale wheat lodging monitoring by band transformation of UAV and Sentinel-2A multispectral imagery. Inf. Process. Agric. 13 (1), 15–25. http://dx.doi.org/10.1016/j.inpa.2025.07.006.

Zhang, G., Yan, H., Zhang, D., Zhang, H., Cheng, T., Hu, G., Shen, S., Xu, H., 2023. Enhancing model performance in detecting lodging areas in wheat fields using UAV RGB imagery: Considering spatial and temporal variations. Comput. Electron. Agric. 214, 108297. http://dx.doi.org/10.1016/j.compag.2023.108297.

Zhao, B., Li, J., Baenziger, P.S., Belamkar, V., Ge, Y., Zhang, J., Shi, Y., 2020. Automatic wheat lodging detection and mapping in aerial imagery to support high-throughput phenotyping and in-season crop management. Agronomy 10 (11), 1762. http://dx.doi.org/10.3390/agronomy10111762.

Zhao, J., Li, Z., Lei, Y., Huang, L., 2023. Application of UAV RGB images and improved PSPNet network to the identification of wheat lodging areas. Agronomy 13 (5), 1309. http://dx.doi.org/10.3390/agronomy13051309.